RESEARCH ARTICLE

Wavelength-selective dual-channel coupling transistor for neuromorphic vision and In-sensor logic

Yurong Jiang*, Jianing Zhang, Suicai Zhang, Xuan Qin, Leiming Yu, Xueping Li, Xiaohui Song, Congxin Xia*

[1] School of Physics, Henan Key Laboratory of Advanced Semiconductor & Functional Device Integration, Henan Normal University, Xinxiang 453007, China

[2] College of Electronic and Electrical Engineering, Henan Normal University, Xinxiang 453007, China

Corresponding authors. E-mail: *jiangyurong@htu.edu.cn, *xiacongxin@htu.edu.cn

Received June 20, 2026; accepted August 18, 2026

Supporting Information

Experimental Section

Phototransistor fabrication processes: First, the Si/SiO_2 substrate with a size of approximately 1 cm×1 cm was cleaned sequentially with acetone, isopropanol, and absolute ethanol. Subsequently, the bottom electrode was designed and fabricated on the 300 nm-thick substrate, the position of the electrode was determined using a maskless lithography machine, and then a 30 nm-thick gold (Au) film was deposited by a thermal evaporation process with a vacuum coating machine. Next, CIPS flake and MoS_2 flake were mechanically exfoliated from bulk crystals (Shanghai Onway Technology Co., Ltd.), and then sequentially transferred onto the bottom electrode using a transfer system (Metatest, E1-G) to form a cross structure. Finally, gold source-drain electrodes were evaporated, completing the fabrication of the device.

Characterization and Measurements: The morphology of the device was characterized using an atomic force microscope (AFM, Bruker Dimension Icon) in tapping mode. Raman spectroscopy measurements were performed with a Horiba LabRAM HR Evolution confocal Raman system under excitation by a 532 nm laser. UV-visible absorption spectra were obtained using quartz substrates with a PerkinElmer Lambda 1050 spectrometer with an integrating sphere. Electrical measurements were carried out using an Agilent B1500A semiconductor parameter analyzer, which enables I-V measurements over a range from 0.1 fA to approximately 1 A. Photocurrent mapping was obtained by scanning the sample under a focused laser (532 nm, with a spot size of approximately 2 μm). Furthermore, all optoelectronic measurements were conducted in air.

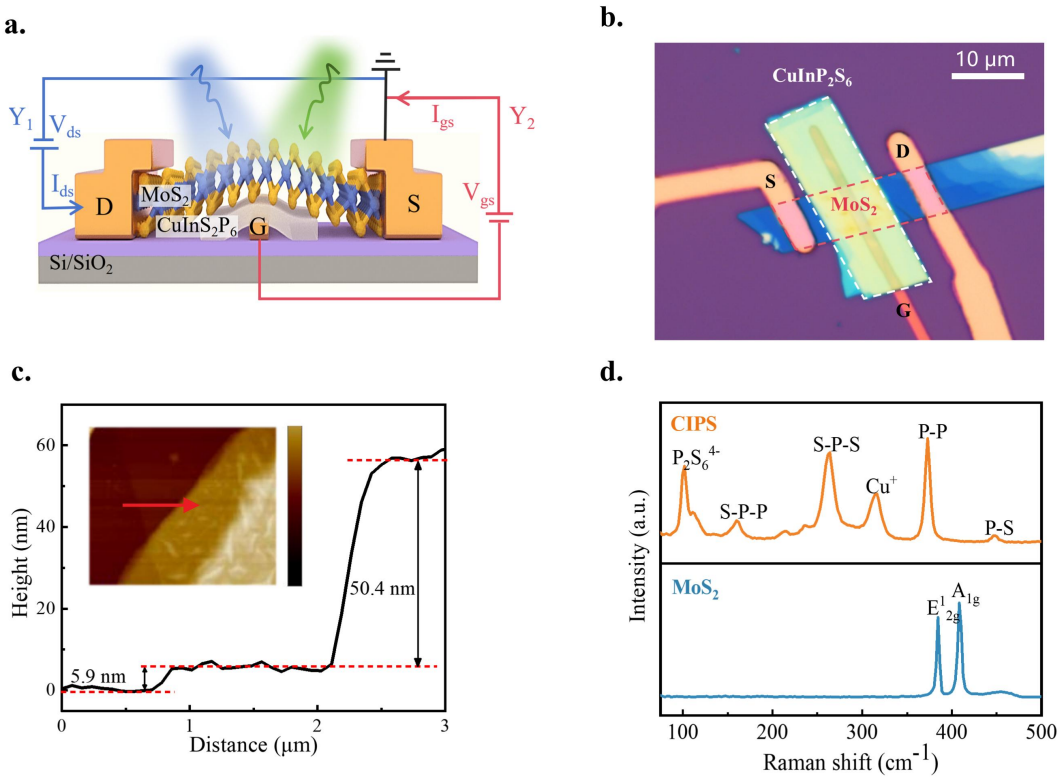


Figure S1. (a) Schematic structure of the dual-channel phototransistor. (b) Optical microscope image. (c) The thicknesses of the MoS_2 and CIPS nanosheets were measured by AFM (inset: morphology image). (d) Raman spectrum of MoS_2 and CIPS nanosheets.

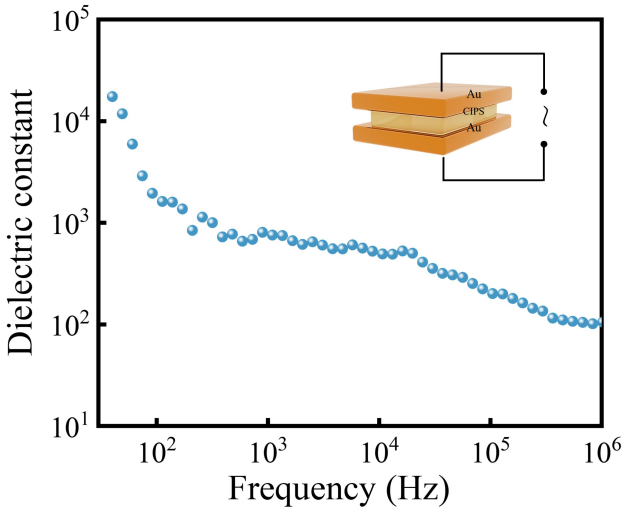


Figure S2. CIPS flake dielectric constant at different frequencies.

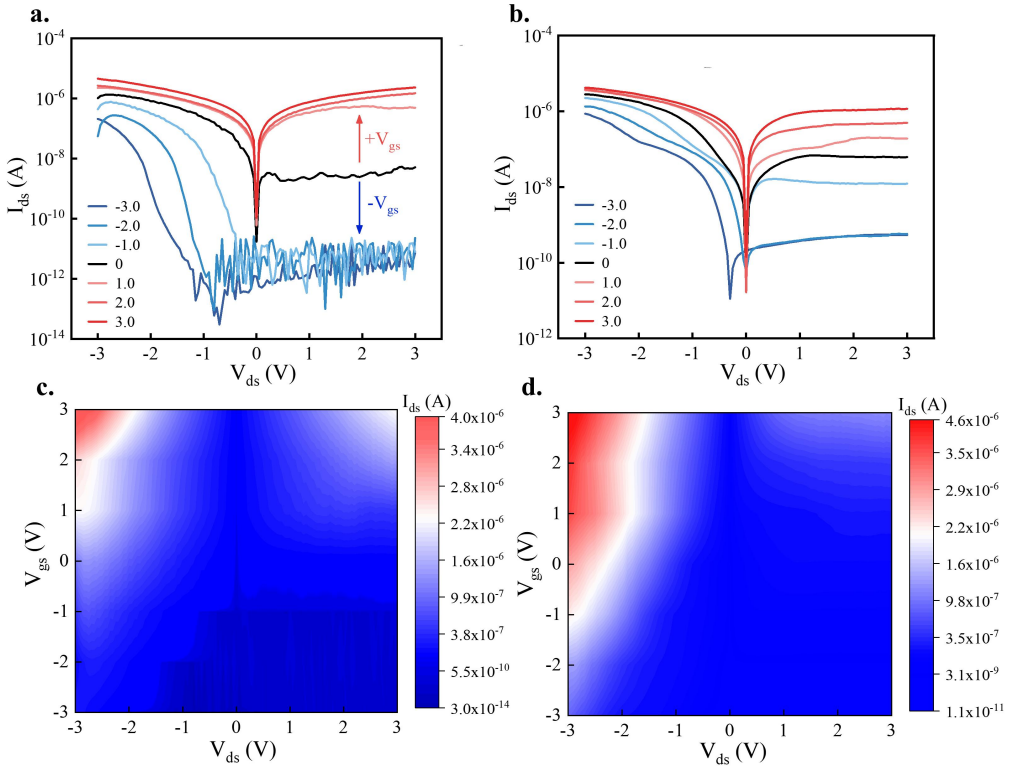


Figure S3. Output characteristics of the phototransistor at various V_{gs} values (a) in the dark and (b) under 405 nm illumination at an optical power density of 24.5 mW cm^{-2}, with the corresponding current heatmaps shown in (c) and (d).

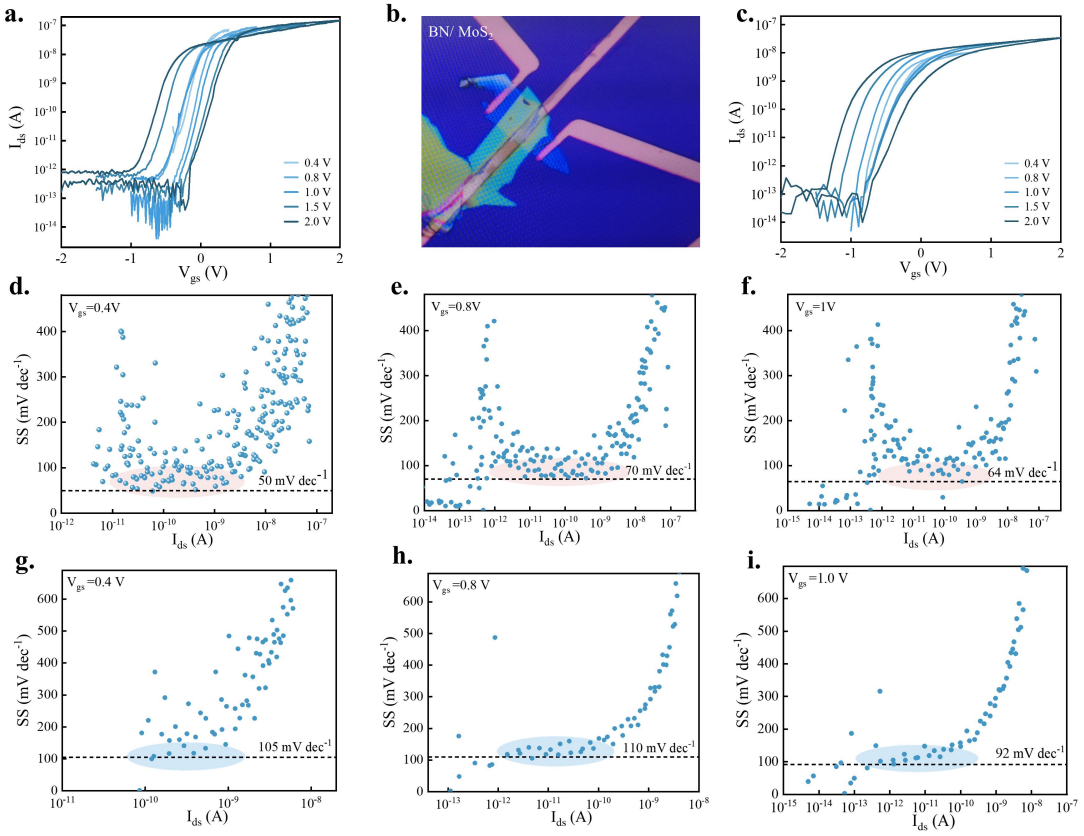


Figure S4. (a) Transfer characteristic curves of the MoS_2/CIPS phototransistor, and the subthreshold swings extracted at V_{gs} = 0.4 V (d), 0.8 V (e), and 1.0 V (f). (b) Optical image of the MoS_2/h-BN phototransistor; (c) its transfer characteristic curves, and the subthreshold swings extracted at V_{gs} = 0.4 V (g), 0.8 V (h), and 1.0 V (i).

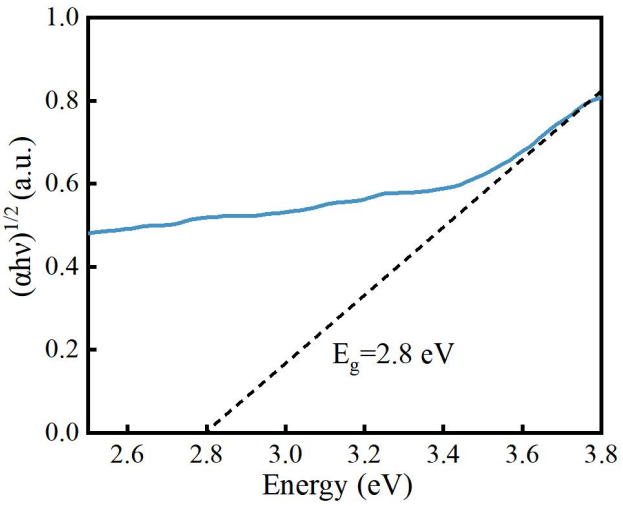


Figure S5. The Tauc plot corresponding to the UV-Vis absorption spectrum shows the optical bandgap of CIPS.

UV-Vis diffuse reflectance spectroscopy of CIPS shows a sharp absorption edge at ~430 nm. Its optical bandgap is calculated as 2.8 eV via Tauc Plot, with the formula given below:

$$(\alpha h\nu)^{(1/n)} = B\,(h\nu - E_g) \qquad (1)$$

where α, h, B and ν are the absorption coefficient, Planck constant, proportional constant and photon frequency, respectively. It should be noted that the value of n for CIPS, an indirect bandgap semiconductor, is 2.

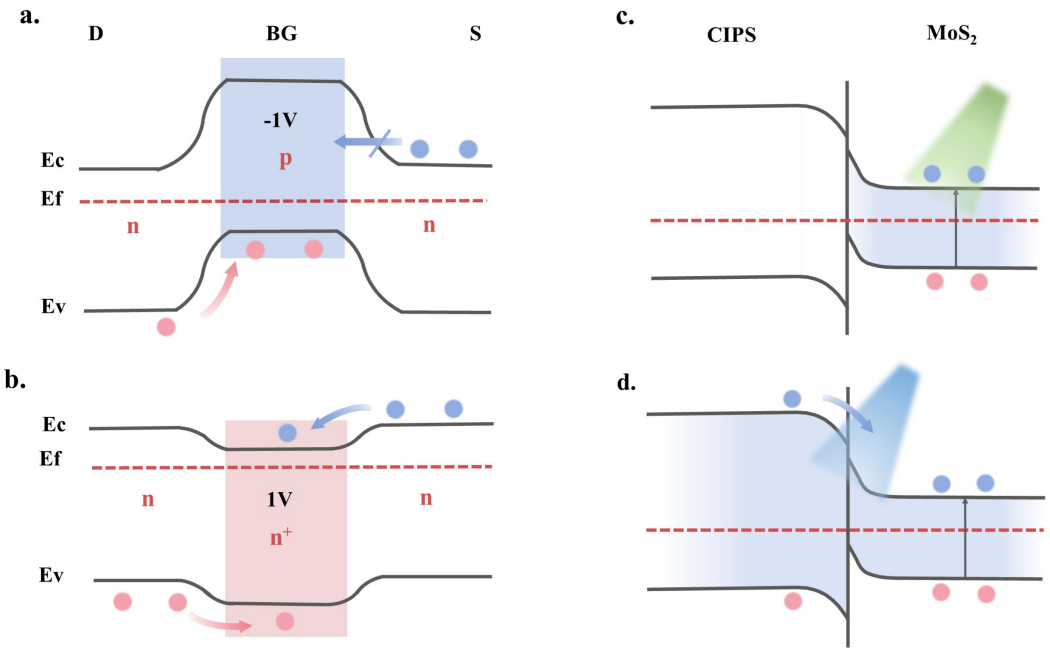


Figure S6. Band diagrams of the heterojunction under (a) negative gate voltage and (b) positive gate voltage in the dark, as well as under (c) 532 nm and (d) 405 nm laser irradiation at negative gate voltage.

Under dark conditions, at V_{gs} = -1 V, hole injection converts the n-type MoS_2 channel into an n-p-n homojunction (Figure S6a), reducing I_{ds}. Conversely, V_{gs} = +1 V injects electrons into MoS_2, yielding an n-n^+-n channel (Figure S6b) and increasing I_{ds}. Under negative V_{gs}, medium-wide bandgap CIPS is inert to 532 nm photons, so photogenerated carriers are exclusively produced in MoS_2, enhancing conductance (Figure S6c). However, 405 nm irradiation induces photoelectron injection from CIPS into the channel, further increasing conductance (Figure S6d).

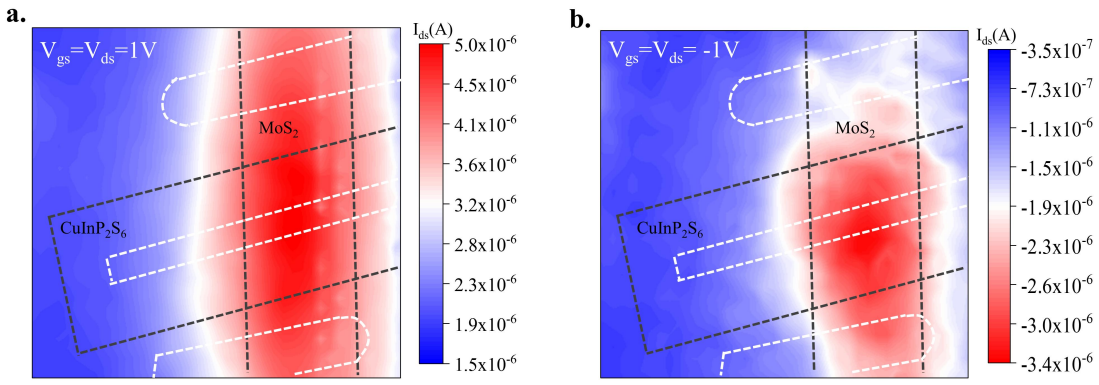


Figure S7. Scanning photocurrent mapping images under light illumination at (a) V_{gs} = V_{ds} = 1 V and (b) V_{gs} = V_{ds} = -1 V.

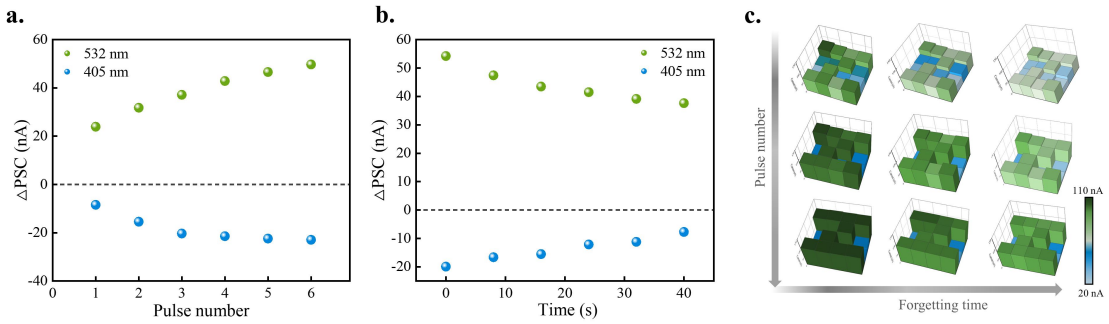


Figure S8. Variations in photocurrent with the number of pulses (a) and decay time (b). (c) Emulation of the color image sensing and memory functions of human vision.

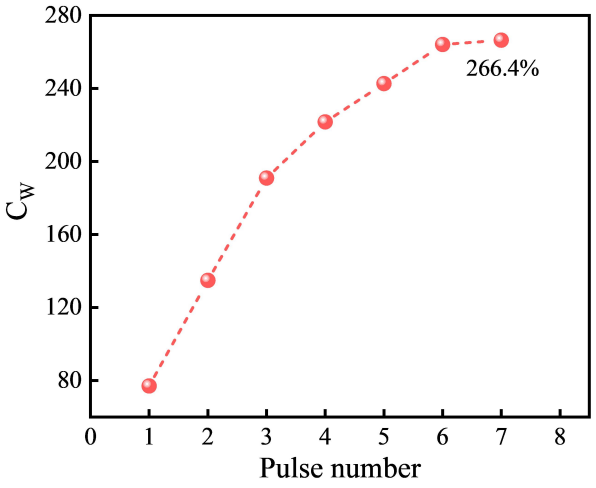


Figure S9. Weber contrast as a function of optical pulse number, calculated from the current responses under 532 and 405 nm illumination.

The formula for calculating Weber contrast is as follows,

$$C_W=\frac{I_{max}-I_{min}}{I_{min}}$$

where I_{max} and I_{min} are the current values generated under 532 nm and 405 nm light illumination, respectively. It can be seen that the contrast gradually increases with increasing pulse number, reaching a maximum of 266.4%.

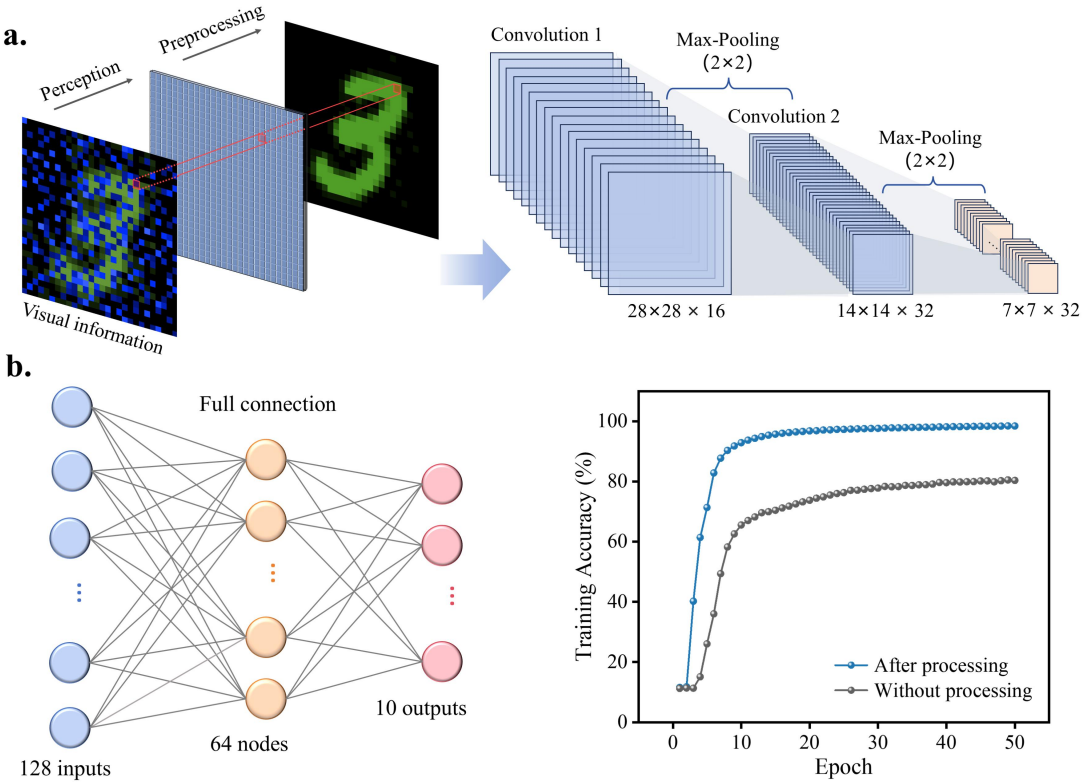


Figure S10. (a) Convolutional neural network based on dual-channel phototransistors for color digit recognition. (b) Structure of fully connected neural network and analysis of recognition accuracy.

This study is based on the MNIST dataset. The green digit "3" is selected as the target recognition pattern, and blue background noise is added to construct the input images. After preprocessing with dual-channel phototransistors, the contrast of the target pattern was effectively enhanced. The preprocessed images were then input into a convolutional neural network (CNN) to achieve accurate recognition of the handwritten digit "3" (Figure S10a). This CNN model consists of two feature extraction layers and a fully connected neural network (FCNN) with a 128 × 64 × 10 structure (Figure S10b). Experimental results show that after 50 epochs of training, the recognition accuracy of the original input images is 80.3%. In contrast, the recognition accuracy of the input images preprocessed by the aforementioned device is significantly improved to 98.4%.

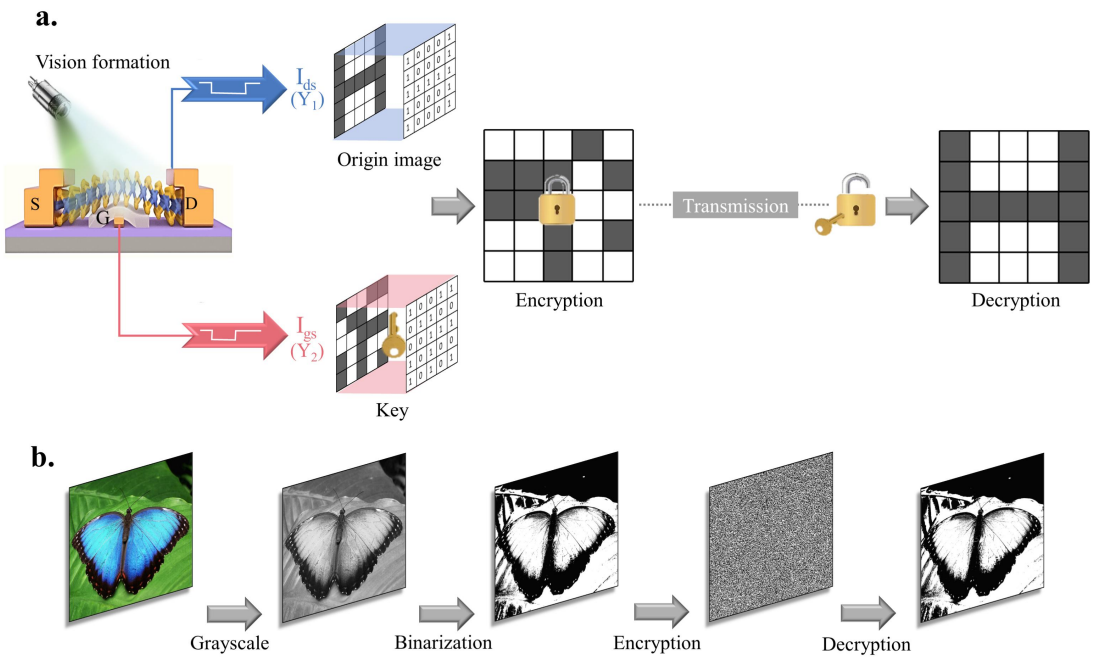


Figure S11. Encryption and decryption of the letter (a) and binarized image (b) using a dual-channel phototransistor.

The half-adder logic based on dual-channel phototransistors enables the encryption and decryption of images (Figure S11a). The "pixels of the plaintext image" and "pixels of the key image" are respectively mapped to the two inputs (A, B) of the half-adder. The XOR logic operation of the half-adder is employed as the core encryption mechanism, and the output Sum result serves as the ciphertext image. This is because the XOR operation possesses reversibility, which meets the requirement of decryption. Meanwhile, the Carry result output by the AND logic acts as auxiliary encryption information, which can be used for double verification to prevent key errors or ciphertext tampering. Here, the letter "H" is used as an example. High-gray-scale pixels correspond to the logic state "1", and low-gray-scale pixels correspond to "0". The logic matrix of "H" is [10001, 01100, 00111, 10001, 10001], and the corresponding key matrix is [10011, 01100, 00111, 10100, 10101]. The encryption matrix C is obtained through A XOR B, and the decryption matrix D is derived from Sum XOR B. To verify the correctness of decryption, the verification matrix E is further obtained by calculating A AND B. If E is equal to Carry, the decryption result is correct. If an attacker tampers with part of the ciphertext or uses an incorrect key, the output matrix D will not match the original Carry, leading to verification failure. The entire process ensures the encryption of the letter and protects the integrity of the decrypted data. Similarly, we have implemented the encryption and decryption of binarized images (Figure S11b).